Biosensors and Bioelectronics 94 (2017) 686–693

Contents lists available at ScienceDirect

Biosensors and Bioelectronics

journal homepage: www.elsevier.com/locate/bios

In situ synthesis of cylindrical spongy polypyrrole doped protonated graphitic carbon nitride for cholesterol sensing application

Bishnu Kumar Shrestha[a,b], Rafiq Ahmad[c], Sita Shrestha[a], Chan Hee Park[a,b,*], Cheol Sang Kim[a,b,*]

[a] Department of Bionanosystem Engineering, Graduate School, Chonbuk National University, 567 Baekje-daero, Deokjin-gu, Jeonju-si, Jeollabuk-do 54896, Republic of Korea
[b] Division of Mechanical Design Engineering, Chonbuk National University, 567 Baekje-daero, Deokjin-gu, Jeonju-si, Jeollabuk-do 54896, Republic of Korea
[c] School of Semiconductor and Chemical Engineering, Nanomaterials Processing Research, Chonbuk National University, 567 Baekje-daero, Deokjin-gu, Jeonju-si, Jeollabuk-do 54896, Republic of Korea

ARTICLE INFO

Keywords:
Polypyrrole
Carbon nitride
Ultra-thin nanosheets
Biocompatible
Cholesterol biosensor

ABSTRACT

Herein, we demonstrate the exfoliation of bulk graphitic carbon nitrides (g-C_3N_4) into ultra-thin (~3.4 nm) two-dimensional (2D) nanosheets and their functionalization with proton (g-$C_3N_4H^+$). The layered semiconductor g-$C_3N_4H^+$ nanosheets were doped with cylindrical spongy shaped polypyrrole (CSPPy-g-$C_3N_4H^+$) using chemical polymerization method. The as-prepared nanohybrid composite was utilized to fabricate cholesterol biosensors after immobilization of cholesterol oxidase (ChOx) at physiological pH. Large specific surface area and positive charge nature of CSPPy-g-$C_3N_4H^+$ composite has tendency to generate strong electrostatic attraction with negatively charged ChOx, and as a result they formed stable bionanohybrid composite with high enzyme loading. A detailed electrochemical characterization of as-fabricated biosensor electrode (ChOx-CSPPy-g-$C_3N_4H^+$/GCE) exhibited high-sensitivity (645.7 μAmM^{-1} cm^{-2}) in wide-linear range of 0.02–5.0 mM, low detection limit (8.0 μM), fast response time (~3 s), long-term stability, and good selectivity during cholesterol detection. To the best of our knowledge, this novel nanocomposite was utilized for the first time for cholesterol biosensor fabrication that resulted in high sensing performance. Hence, this approach opens a new prospective to utilize CSPPy-g-$C_3N_4H^+$ composite as cost-effective, biocompatible, eco-friendly, and superior electrocatalytic as well as electroconductive having great application potentials that could pave the ways to explore many other new sensors fabrication and biomedical applications.

1. Introduction

Tremendous approaches have been endorsed to prevent, reduce and treat the life-threatening dyslipidemia and cardiovascular diseases such as hypertension, atherosclerosis and cardiopathy (Baigent et al., 2010; Arsenault and Puri, 2016). The undesirable accumulation of cholesterol is the main cause of such disease, which is due to excessive use of cholesterol-containing food, lack of regular physical activities, and tobacco smoking. At present, there is substantial increase in number of patients suffering from heart and stroke related diseases that attracted more attention and challenges in global health for the coming decades (Labarthe and Dunbar, 2012). Thus, constant monitoring of blood cholesterol level is required for early clinical diagnostic and treatment.

Development and utilization of highly specific, low-cost, scalable, biocompatible, and eco-friendly cholesterol biosensors are required as promising biomedical devices to replace the commonly used time consuming expensive equipment's (Saxena and Das, 2016). In this context, an extensive research work has been performed for the fabrication of effective biosensor architecture to monitor cholesterol level with fast response time (Komathi et al., 2016). Among variety of reported techniques and strategies for cholesterol detection, an electrochemical based method has received significant interest as an easy, high sensitivity, fast response time, cost-effective, and highly accurate during measurement (Ahmadalinezhad and Chen, 2011; Fang et al., 2006; Mansano et al., 2010; Ahmad et al., 2013, 2014; Labib et al., 2016). Enzyme based electrochemical cholesterol biosensors are specific, accurate and significantly enhance biocatalytic reaction during analyte detection (Wilson and Hu, 2000). However lack of appropriate micro/nanostructures and properties of composite matrix, the redox active sites of immobilized enzyme lower its performance and hinder the electrode efficiency for direct and fast electron transport. To

* Corresponding authors at: Department of Bionanosystem Engineering, Graduate School, Chonbuk National University, 567 Baekje-daero, Deokjin-gu, Jeonju-si, Jeollabuk-do 54896, Republic of Korea.
E-mail addresses: biochan@jbnu.ac.kr (C.H. Park), chskim@jbnu.ac.kr (C.S. Kim).

http://dx.doi.org/10.1016/j.bios.2017.03.072
Received 28 December 2016; Received in revised form 20 March 2017; Accepted 29 March 2017
Available online 04 April 2017
0956-5663/

enhance the performance of enzyme based biosensors, various nanomaterials including metals and metal oxides, graphene, chitosan, and carbon nanotubes, semiconductors nanocrystals and quantum dot (QDs) have been employed as nanocomposite materials (Tan et al., 2005; Hahn et al., 2012). Despite intensive research efforts on extensive exploitation of metal and metal oxide nanoparticles, remarkable challenges still remain such as dispersion, less economical, hard to modify their surface, and ecological concerns while being used in biological applications (Medintz et al., 2005; Somers et al., 2007).

Taking all these facts into consideration, organic conducting polymers (OCPs) have been paid noteworthy attention for various applications as a consequence of their highly conductive, biocompatible, cost-effective, easily-copolymerization, and environment friendliness properties (Aydemir et al., 2016; Malhotra et al., 2006; Quigley et al., 2009; Yuan et al., 2013). Additionally, π-conjugated backbone in OCPs enhance electrical conductive pathway which would facilitate the charges transport process (Ahuja et al., 2007). Among many OCPs, polypyrrole (PPy) as an intrinsic OCP has been widely recognized electron transfer material for unconditional grafting into hybrid materials and spineless bipolarons state, which demonstrated the interesting application for biosensors (Bredas and Street, 1985). Additionally, varied surface morphologies (tubular, nanowires, globular, and cylindrical) of oxidized PPy inherits pivotal roles in redox activities, strong biocompatibility, and non-toxic towards biomolecules (Sadki et al., 2000; Qian et al., 2014; Shrestha et al., 2016; Brahim et al., 2001). Previously, oxidized PPy nanostructures integrated with ChOx has been reported for cholesterol detection. The bioengineered composite materials of PPy can be obtained by chemical and electrochemical polymerization, which are regarded as a fast, effective and ideal strategy for biosensor fabrication to detect cholesterol. Despite its attractive sensing applications, none of the studies have been explored the utilization of PPy nanostructures with graphitic carbon nitride (g-C_3N_4) to make nanohybrid composite material.

In recent few years, metal-free, bio-functional 2D materials have opened up exciting possibilities for the development of amperometric cholesterol biosensors due to their unique electrical, optical, mechanical, chemical and topographical properties (Ramendra and Raj, 2010). Polymeric g-C_3N_4, a 2D nanosheet analogous of graphene has triggered keen interest because of biocompatibility, less expensive, easy to synthesize, semiconductor behavior with appropriate band gap energy and large surface area to volume ratio. Thus, their potential application as catalyst, and energy transducer employed as best ideal substrate in biosensor platforms (Wang et al., 2009; Lu et al., 2017; Xiong et al., 2017). Owing to the nitrogen-doped, the g-C_3N_4 showed strong mechanical and good electrical properties and also exhibited robust thermal and chemical stability, which ensured key interest for sensing applications (Lu et al., 2015; Zhang et al., 2010). The presence of large number of tri-s-triazine units in g-C_3N_4 also confirms the high thermal stability. Even though, their inter layers interactions hold g-C_3N_4 insoluble in most water and organic solvents (Shi et al., 2016). Recently, Niu et al. synthesized ultra-thin nanosheets of mesoporous g-C_3N_4 with high surface area by chemical and thermal oxidation etching and liquid exfoliation in polar solvent for improved photocatalytic activities (Niu et al., 2012; Bai et al., 2014). Zhang et al. and Wang et al. reported improvement in homogenous dispersibility through surface functionalization of g-C_3N_4 by iodine and sulfur doping, respectively (Zhang et al., 2014; Wang et al., 2015). Furthermore, Fang et al. used Pd/Au bimetallic nanoparticles to decorate the g-C_3N_4 nanosheets to enhance the catalytic performance (Fang et al., 2016). Importantly, there are no reports offering cholesterol biosensor fabrication utilizing CSPPy modified ultra-thin 2D g-C_3N_4 nanosheets for cholesterol detection.

In this work, we report, for the first time, synthesis of highly efficient and desirable nanohybrid composite of CS shaped PPy doped protonated ultra-thin g-$C_3N_4H^+$ nanosheets. Subsequently, ChOx was immobilized onto nanohybrid composite (CSPPy-g-$C_3N_4H^+$) to construct cholesterol biosensor (ChOx-CSPPy-g-$C_3N_4H^+$/GCE) electrode. As a consequence, our designed cholesterol biosensor exhibited improved electrochemical sensing performance. We believe that our results will lead a guiding role to design a metal-free, label-free, non-toxic, cost-effective and electrochemically active bio-sensing electrode.

2. Experimental section

2.1. Proton functionalization of g-C_3N_4 (g-$C_3N_4H^+$)

Bulk g-C_3N_4 in heterogeneous aqueous suspension was employed in probe sonication for 4 h to obtain fine exfoliated ultra-thin nanosheets. The complete protonation was performed under reflux heating at 70 °C for 4 h with constant stirring. Prior to reflux in condenser, 0.5 g g-C_3N_4 ultra-thin nanosheets were dispersed in 100 mL of concentrated HCl and sonicated for 30 min. Then, the product was allowed to cool down to room temperature followed by dilution and continuous washing with distilled water and anhydrous ethanol during filtration. Finally, the obtained light yellow residue of proton functionalized g-C_3N_4 (g-$C_3N_4H^+$) was dried overnight at 80 °C (Ong et al., 2015).

2.2. Preparation of CSPPy doped g-$C_3N_4H^+$(CSPPy-g-$C_3N_4H^+$) nanohybrid composite

To dope the g-$C_3N_4H^+$ with CSPPy, first, 0.25 g of engineered g-$C_3N_4H^+$ nanosheets were added into 100 mL of 1 M aqueous acetonitrile solution containing 0. 01 M pyrrole and sonicated for 30 min. Then, the suspension was treated with 0.01 M ammonium persulfate in flask at 5 °C for 24 h, while stirring at constant speed (Scheme 1a). Complete oxidative chemical polymerization of pyrrole produces bipolaron state of PPy in cylindrical shape deposited on the surface of g-$C_3N_4H^+$ nanosheets. Finally, as-prepared CSPPy-g-$C_3N_4H^+$ nanohybrid composite was filtered and washed several time with anhydrous ethanol and distilled water, respectively, and dried overnight at 70 °C.

2.3. Fabrication of cholesterol biosensor (ChOx-CSPPy-g-$C_3N_4H^+$/GCE) electrode

To fabricate cholesterol biosensor, first, bare glassy carbon electrode (GCE; 3 mm in diameter) was polished successively with 0.3 μm and 0.05 μm particle sizes of alumina suspensions followed by 1 μm particle size of diamond suspension on rayon polishing pad to obtain mirror finishing of GCE surface. All polishing steps were followed by sonication in ethanol for 15 min and extensive rinsing with anhydrous ethanol and deionized water. The cleaned GCEs were treated by CV technique in the potential range from −0.2 to 1.0 V (vs. SCE) using 0.5 M H_2SO_4 as

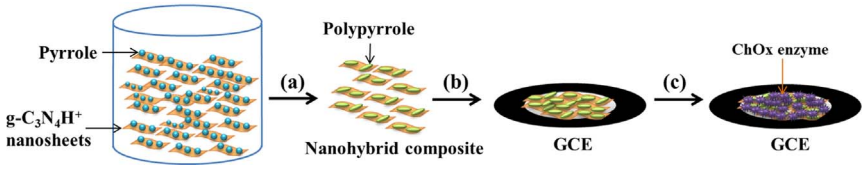

Scheme 1. Schematic illustration of (a) one-step in situ chemical polymerization of PPy on g-$C_3N_4H^+$ nanosheets, (b) deposition of hybrid composite on GEC, and (c) ChOx enzyme immobilization by physical adsorption method to fabricate cholesterol biosensor electrode.

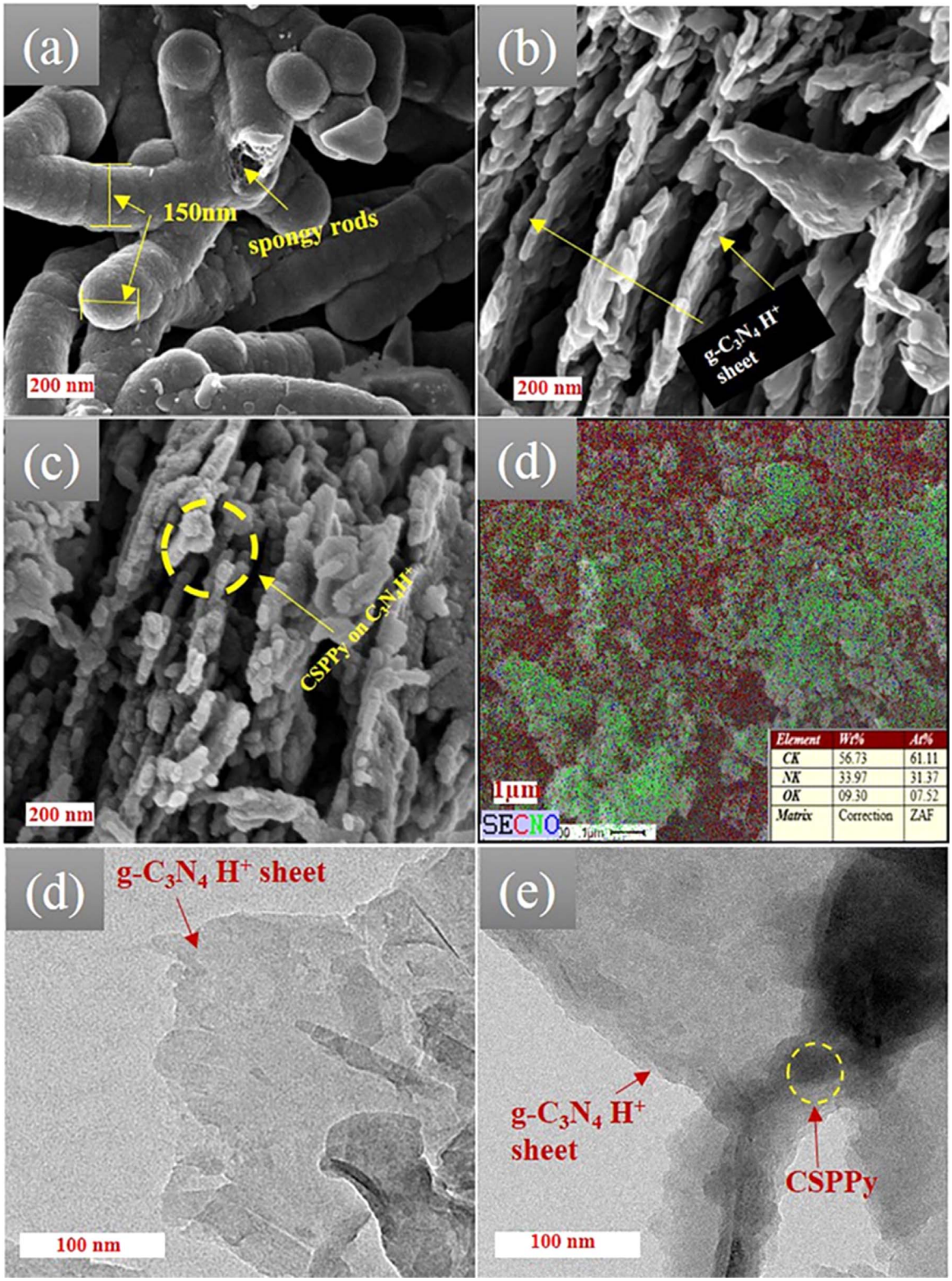

Fig. 1. FESEM image of (a) oxidized CSPPy, (b) g-$C_3N_4H^+$, (c) CSPPy-g-$C_3N_4H^+$, and (d) elemental mapping of CSPPy-g-$C_3N_4H^+$ nanohybrid composite with EDX spectrum (inset); and CS-Corrected-FETEM/STEM image of (e) g-$C_3N_4H^+$ ultra-thin nanosheets (f) CSPPy-g-$C_3N_4H^+$ nanohybrid composite.

electrolytes till the obtained cyclic voltammograms curves were not constant and followed by drying under nitrogen stream. Then, 0.5 mg CSPPy-g-$C_3N_4H^+$ nanohybrid composite mixed with 3 µL of ethylene glycol was casted on the GCE surface and dried at 50 °C for 30 min (Scheme 1b). In the next step, 5 µL of ChOx (5 mg/mL) prepared in 0.1 M PBS (pH 7.4) was immobilized on the CSPPy-g-$C_3N_4H^+$/GCE electrode surface by physical adsorption method (Scheme 1c). Finally, the biosensor electrodes (ChOx-CSPPy-g-$C_3N_4H^+$/GCE) were washed with PBS to remove loosely attached enzymes and kept at 4 °C under dry condition while not in use. The optimization studies were performed to investigate the optimized parameters (i.e. enzyme concentration, PPy concentration, amount of CSPPy-g-$C_3N_4H^+$ on GCE, and ChOx immobilization time) for high-performance cholesterol biosensor fabrication (for details see Supplementary material and Fig. S1-S4).

3. Results and discussion

3.1. Structural characterizations

Fig. 1a-d show the FESEM images of (a) oxidized CSPPy, (b) g-$C_3N_4H^+$, (c) CSPPy-g-$C_3N_4H^+$, and (d) elemental mapping of CSPPy-g-$C_3N_4H^+$ nanohybrid composite with EDX data (inset). From Fig. 1a, the controlled chemical polymerization of pyrrole resulted into cylindrical spongy shaped PPy (CSPPy) with uniform diameter (~150 nm) and smooth surface topography. Noted that CSPPy exists in porous, smooth, straight with cylindrical geometry and increase in thin film conjugation may accelerate the mobility of electrons and charges resulting improve in electrical conductivity of CSPPy. The exfoliation and HCl treatment of bulk g-C_3N_4 resulted it into g-$C_3N_4H^+$ nanosheets like structures (Fig. 1b), which have more lamella sheaths in layer-by-layer configuration that provides high surface area exposed with surface edge defects due to proton functionalization. In addition, homogenous protons functionalization not only changes the surface morphologies but also alters their electronic structures and significantly enhanced the ionic and electronic conductivity (Zhang et al., 2009). The chemically synthesized nanohybrid composite material (CSPPy-g-$C_3N_4H^+$) showed uniform incorporation of oxidized CSPPy on g-$C_3N_4H^+$ nanosheets (Fig. 1c). It could be suggested that p-type PPy in the form of bipolaron state can be easily attracted towards nitrogen rich g-$C_3N_4H^+$. The chemical doping of such p-type CSPPy is an innovative strategy to reduce the band gap of semiconducting material (g-$C_3N_4H^+$) to use as metal-free electrocatalytic conductive material (Gong et al., 2009). Additionally, the elemental mapping shows C and N peaks along with oxygen (O) peak. The presence of O peak is due to the protonation of g-C_3N_4 during acid treatment. Importantly, the proton-rich g-$C_3N_4H^+$ material is endowed with high dispersibility in the polar solvent. From CS-Corrected-FETEM/STEM images, nearly transparent ultra-thin nanosheets of g-$C_3N_4H^+$ can be seen (Fig. 1e). However, CSPPy doped g-$C_3N_4H^+$ nanohybrid composite (Fig. 1f) illustrates the uniformly decoration of CSPPy within inner laminal nanosheets of g-$C_3N_4H^+$ to form bipolymeric conjugation resulting mechanically stable nanocomposite material (CSPPy-g-$C_3N_4H^+$). Furthermore, the CS-Corrected-FETEM/STEM and AFM images verify the formation of ultra-thin nanosheet (~3.4 nm) of g-$C_3N_4H^+$(Fig. S5; supporting information). Also, obtained thickness is in agreement with previously reported value of 2–4 nm (Ma et al., 2014).

Fig. 2(i) presents the typical XRD spectra of oxidized CSPPy, bulk g-C_3N_4, g-$C_3N_4H^+$, and CSPPy-g-$C_3N_4H^+$. The XRD spectrum of CSPPy shows a broad peak at 26.4°, which is assigned to the amorphous property of PPy resulting from pyrrole ring chain (black curve). However, bulk g-C_3N_4 exhibits an intense diffraction XRD peak at 27.41° originated from interlayer diffraction (002) of graphite like structure corresponding to the interlayer spacing of 0.326 nm (red curve). Additionally, a lower angle diffraction peak at 13.1° (d =0.663 nm) was observed, which is due to the face-to-face stacking parallel to c-axis (100) measured from in-planar repeated unit of tri-s-triazine unites (Ma et al., 2014). After protonation of bulk g-C_3N_4, g-$C_3N_4H^+$ showed less pronounced peak intensities, which can be attributed to increase in disorder at the edge of lattice planes and decrease in planar size of tri-s-triazine (blue curve). Also, a small shift in peak orientation from 27.4° to 27.8° indicates the decrease in distance between each nanosheets corresponding to the successful exfoliation of g-$C_3N_4H^+$(Kofuji et al., 2016). It was noteworthy that the noticeable decrease in the peak intensity of g-$C_3N_4H^+$ as compared to bulk g-C_3N_4 also reveals the formation of ultra-thin layered nanosheets morphology. In addition, oxidized CSPPy doped on g-$C_3N_4H^+$ has no significance effect on XRD spectra of nanohybrid composite material (data not shown).

Fig. 2(ii) shows the FT-IR spectra recorded form oxidized CSPPy (a), bulk g-C_3N_4 (b), g-$C_3N_4H^+$(c), and CSPPy-g-$C_3N_4H^+$(d). The

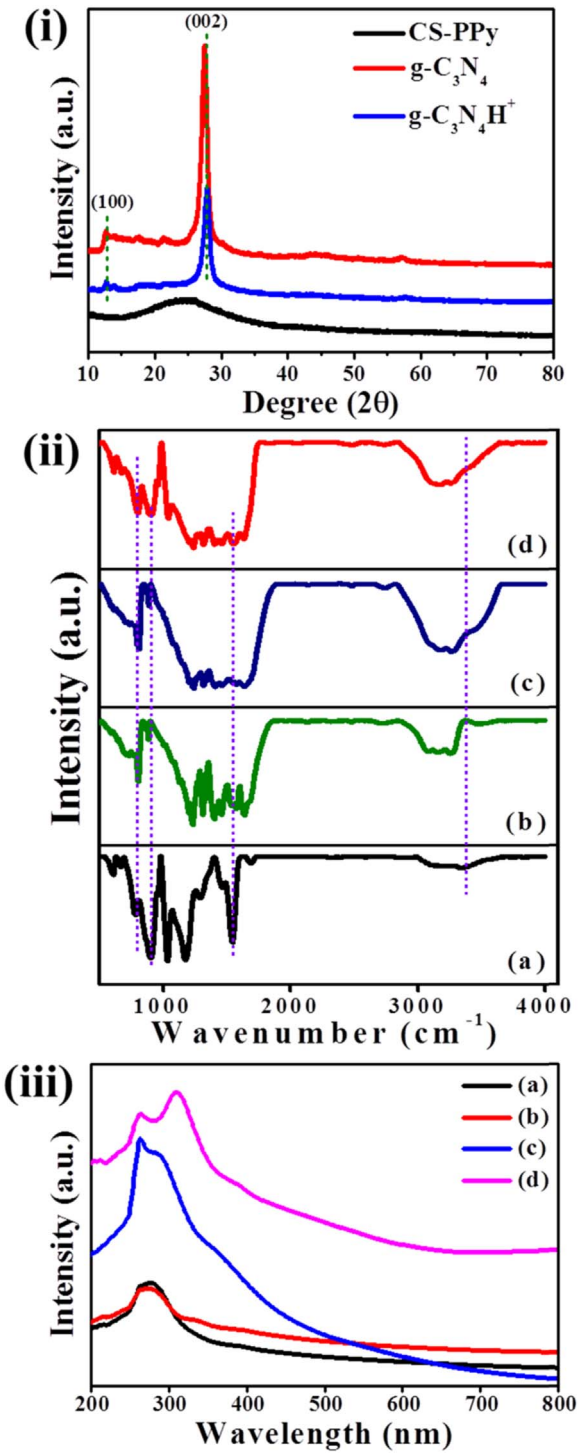

Fig. 2. (i) XRD pattern of CSPPy (black curve), g-C_3N_4 (red curve), and g-$C_3N_4H^+$(blue curve); (ii) FT-IR spectra of (a) CSPPy, (b) g-C_3N_4 (c) g-$C_3N_4H^+$ nanosheets (d) CSPPy-g-$C_3N_4H^+$; (iii) UV–vis absorption spectra of g-C_3N_4 (a), g-$C_3N_4H^+$(b), CSPPy (c), and CSPPy-g-$C_3N_4H^+$(d).

oxidized CSPPy spectrum (a) shows broad bands at ~1400–1600 cm^{-1} corresponding to C=C and C-C bonds stretching. Peaks appeared at 906 cm^{-1} and 1086 cm^{-1} are assigned to C-H out-of-plane deformation and bending mode, respectively (Li et al., 2010). The bulk g-C_3N_4 (b) and g-$C_3N_4H^+$(c) show peak at 806 cm^{-1} that is originated from tri-s-triazine and assigned as breathing mode of aromatic hetero cycle in C-N ring system. Even more peaks from 1217 to 1647 cm^{-1} correspond to C=N and C-N bonds stretching vibration mode suggesting the highly copolymerizes tri-s-triazine chain and broad peak from

3050 to 3250 cm^{-1} assigned to N-H stretching in secondary and primary amines (Lotsch et al., 2007). In curve c, a broad peak appeared at 3450 cm^{-1} of g-$C_3N_4H^+$ could have existed due to the formation of -OH bonds between moisture content in air and protonated group on g-$C_3N_4H^+$. The lower peaks appeared at 904 cm^{-1} (C-H wagging) and 3350 cm^{-1} (amine groups) in the composite material confirms the successful integration of CSPPy within the g-$C_3N_4H^+$ nanosheets (d).

The optical properties of CSPPy (a), bulk g-C_3N_4 (b), g-$C_3N_4H^+$(c), and CSPPy-g-$C_3N_4H^+$(d) were studied by UV–vis absorption spectra, as shown in Fig. 2(iii). The blue-shift occurred for protonated g-C_3N_4 (g-$C_3N_4H^+$) as compared to bulk g-C_3N_4 from 465 to 417 nm, which confirms the optical band gap associated with semiconducting properties of the protonated g-C_3N_4 nanosheets due to quantum confinement effect (Zhang et al., 2009). The oxidized CSPPy showed peak at 290 nm (π-π*). However, in composite material (CSPPy-g-$C_3N_4H^+$) peak intensity can be observed at 312 nm (n-π*), which may be resulted from two photons excitation during the formation of coordinate covalent bonds between hetro-nitrogen in PPy and H^+ of g-$C_3N_4H^+$ suggesting that the composite is also visible light active. The remarkable red shift and high peaks intensity explain the narrowing of energy band gap due to the extension of π-conjugation system resulting in the enhancement of electrical conductivity of g-$C_3N_4H^+$ semiconductor.

3.2. Electrochemical characterization of modified electrodes

3.2.1. EIS measurements

To characterize the features of surface modified electrodes, EIS technique was employed and obtained data were depicted in Fig. 3(i). The curves manifested a semicircular portion at higher frequencies and linear portion at lower frequencies, which quantify the electron transfer limited process at surface modified electrode and diffusion process, respectively. The charge transfer resistance (R_{CT}) values of g-$C_3N_4H^+$/GCE (741 Ω, curve a), CSPPy/GCE (112 Ω, curve c), and CSPPy-g-$C_3N_4H^+$/GCE (149 Ω, curve e) were recorded. After ChOx immobilization, R_{CT} value of each biosensor electrode substantially increased, as obtained for (ChOx-g-$C_3N_4H^+$/GCE (1569 Ω, curve b), ChOx-CSPPy/GCE (187 Ω, curve d) and ChOx-CSPPy-g-$C_3N_4H^+$/GCE (316 Ω, curve f), which affects both electron transport rate as well as diffusion process. Importantly, oxidized CSPPy (positively charged particle) was doped on protonated g-$C_3N_4H^+$ by Van der Waals repulsion force. Hence, electron rich CSPPy could donate electrons to the conduction band of g-$C_3N_4H^+$ and these donated electrons further participate into the transport process, which suddenly lowers the resistivity of CSPPy-g-$C_3N_4H^+$ nanohybrid composite (Shklovskii and Efros, 2013). The increase in the conductivity of the composite was consistence with the lowering in band gap as illustrated through red shift in UV–vis spectra of the nanohybrid composite film.

3.2.2. Electrochemical measurements of different electrodes

To investigate the electrochemical characterization of the all surface modified electrodes, typical CV response was measured in the potential range from −0.2 to +0.8 V (vs. SCE) at scan rate of 50 mV/s in 5 mM $Fe[CN]_6^{3-/4-}$ solution containing 0.1 M KCl, as shown in the Fig. 3(ii). A well-defined CV curves with diffusion controlled redox process were obtained for each modified electrodes. A higher redox peak current (curve a_1 =216 μA) was obtained from CSPPy-g-$C_3N_4H^+$/GCE, which is higher than the current obtained other two electrodes i.e. CSPPy/GCE (curve b_1 =47 μA) and g-$C_3N_4H^+$/GCE (curve c_1 =23 μA). Importantly, ultra-thin sheets of exfoliated g-$C_3N_4H^+$ persuade enough catalytic active surface area and their chemically doped CSPPy/g-$C_3N_4H^+$ interface could be expected to significantly enhance the electron transfer rate in CSPPy-g-$C_3N_4H^+$, which remarkably decrease the average peak-peak separation (ΔEp =93 mV). The large active surface area typically effect on reaction kinetic of bulk solution on CSPPy-g-$C_3N_4H^+$/GCE composite film and indicates a quite quasi-reversible redox process with increased redox current response. Nevertheless, the

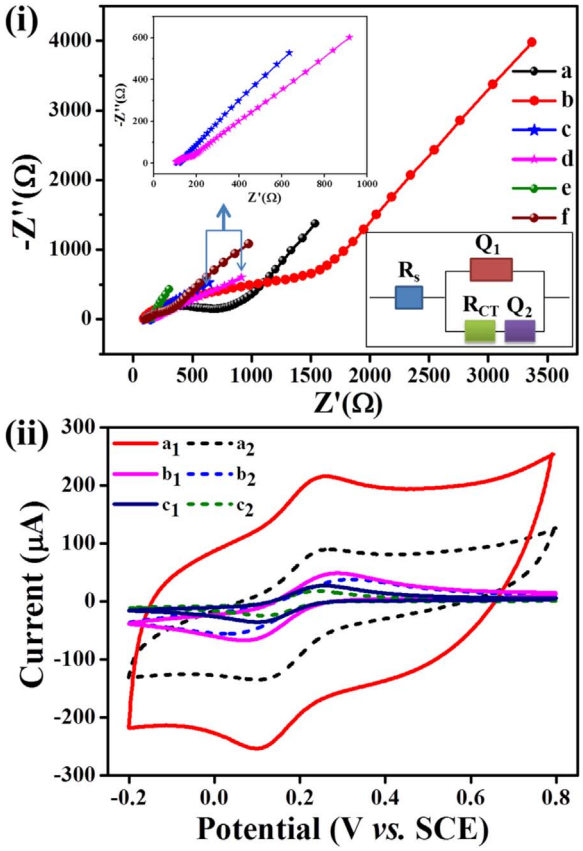

Fig. 3. (i) Nyquist plot of (a) g-$C_3N_4H^+$/GCE, (b) ChOx-g-$C_3N_4H^+$/GCE, (c) CSPPy/GCE, (d) ChOx-CSPPy/GCE, (e) CSPPy-g-$C_3N_4H^+$/GCE, and (f) ChOx-CSPPy-g-$C_3N_4H^+$/GCE in 5 mM K_3Fe $[CN]_6$ with 0.1 M KCl solution. Upper and lower insets show the EIS spectra of GCE modified with composite material before (brown curve) and after (green curve) ChOx immobilization and Randles equivalent circuit, respectively. The Nyquist plots were fitted using Randles equivalent circuit model, which includes parameters like double layered capacitance (Q_1), Warburg impedance (Q_2), electrolytes resistance (R_s), and charge transfer resistance (R_{CT}). (ii) CVs of modified electrodes (a_1) CSPPy-g-$C_3N_4H^+$/GCE, (a_2) ChOx-CSPPy-g-$C_3N_4H^+$/GCE, (b_1) CSPPy/GCE, (b_2) ChOx-CSPPy/GCE, (c_1) g-$C_3N_4H^+$/GCE, and (c_2) ChOx-g-$C_3N_4H^+$/GCE in 5 mM K_3Fe $[CN]_6$ with 0.1 M KCl solution.

oxidized CSPPy has tendency to hold large amount of ChOx in nanohybrid composite, which could be suitable avenue for strong immobilization of ChOx. The immobilization of ChOx reduces the active surface area and forms a blocking layer for diffusion of $Fe[CN]_6^{3-/4-}$ to electrode surface. As a result, after ChOx immobilization both anodic and cathodic peak currents of ChOx-CSPPy-g-$C_3N_4H^+$/GCE (curve a_2 =87 μA), ChOx-CSPPy/GCE (curve b_2=27 μA), and ChOx-g-$C_3N_4H^+$/GCE (curve c_2 =13 μA) are significantly decreased. The ChOx immobilization not only slowdown the electron transfer rate due to decrease in surface area but also created the repulsive force between similar negatively charged ChOx and reduced $Fe[CN]_6^{3-/4-}$, which further lowers the diffusion of electrolyte on electrode surface. Furthermore, the detailed electrochemical kinetic behavior of ChOx-CSPPy-g-$C_3N_4H^+$/GCE was investigated by measuring CV response at different scan rates (25–250 mV/s), as shown in supporting information (Fig. S6a). The obtained well-defined redox peak current response was linearly proportional to the square root of scan rate (Fig. S6b), which suggests that electron transfer process during redox reaction on fabricated electrode, is a diffusion control reaction. In addition, the anodic and cathodic peak currents shift toward positive and negative potential with increase in scan rates indicating a quasi-reversible electron transfer reaction on electrode surface. In addition, the large energy band gap (~ 2.97 eV) of bulk g-C_3N_4 could not favor it as an electrical conductive material. However,

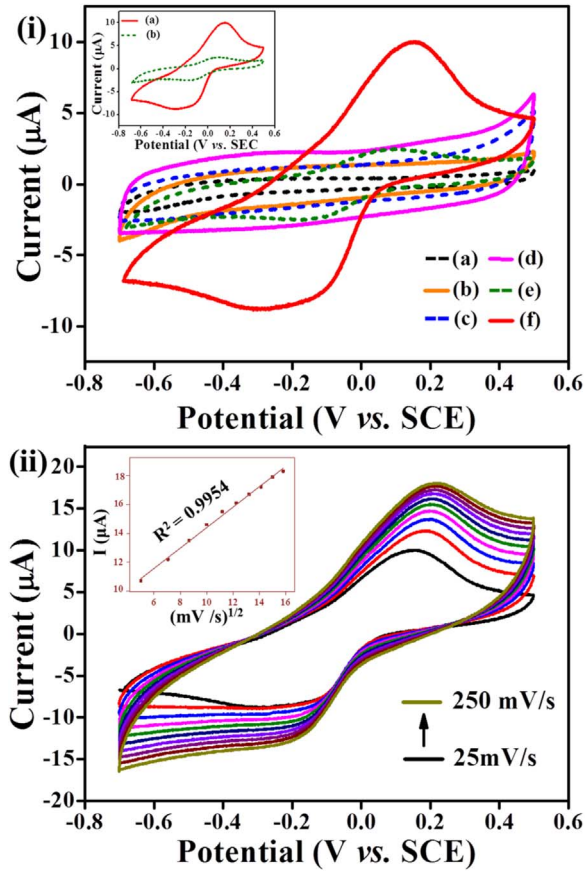

Fig. 4. (i) CVs of modified electrodes i.e. (a) g-$C_3N_4H^+$/GCE, (b) ChOx-g-$C_3N_4H^+$/GCE, (c) CSPPy/GCE, (d) ChOx-CSPPy/GCE, (e) CSPPy-g-$C_3N_4H^+$/GCE, and (f) ChOx-CSPPy-g-$C_3N_4H^+$/GCE in 0.1 M PBS (pH 7.4) before ChOx immobilization (dash lines) and after ChOx immobilization (solid lines) in the presence of 0.05 mM cholesterol at 25 mV/s scan rate. (ii) CVs of ChOx-CSPPy-g-$C_3N_4H^+$/GCE in 0.1 M PBS (pH 7.4) containing 0.05 mM cholesterol at different scan rates (25–250 mV/s). Inset (i) and (ii) show the CV response of only ChOx-CSPPy-g-$C_3N_4H^+$/GCE in the absence and presence of cholesterol and calibration curves of anodic peak current vs. square root of scan rate, respectively.

Niu et al. recently reported that the ultra-thin nanosheet obtained from exfoliation offers better electron mobility rate along with in-plane direction of the nanosheet (Niu et al., 2012). Moreover, high specific surface area of 2D nanosheets forms hydrogen bonds at defective edge of lattice sites during protonation, which can ensure the good electron and charge carrier pathways. Also, their ability to combine with p-type CSPPy material through π-conjugated bonds along polymer chain enhances conductivity of CSPPy-g-$C_3N_4H^+$ composite films (Cao et al., 2015).

3.2.3. Electrocatalytic oxidation of cholesterol on modified electrode

Fig. 4(i) shows CV curves obtained from the electrocatalytic oxidation of cholesterol at different surface modified electrodes before and after ChOx immobilization in the presence of 0.05 mM cholesterol at 25 mV/s scan rate in the applied potential range from −0.7 to +0.5 V (vs. SCE). No obvious oxidation peaks were observed for g-$C_3N_4H^+$/GCE (curve a) and CSPPy/GCE (curve c) electrodes. However, these two electrodes showed a little higher current after ChOx immobilization on the electrode materials i.e. ChOx-g-$C_3N_4H^+$/GCE (curve b) and ChOx-CSPPy/GCE (curve d). This reveals that CSPPy and g-$C_3N_4H^+$ separately have no catalytic effect on the reaction process for cholesterol detection, even after ChOx immobilization. However, CSPPy doped g-$C_3N_4H^+$ nanohybrid modified GCE (curve e) shows a weak oxidation peak current (2.1 μA). This can be attributed to the uniform polymerization of pyrrole on g-$C_3N_4H^+$ nanosheets, which maintains a bridge with ultra-thin sheets and increases both conductivity and electron density of CSPPy-g-$C_3N_4H^+$ nanohybrid composite (Wu et al., 2015). After enzyme immobilization, the oxidation current of ~10.28 μA at +0.17 V was obtained for ChOx-CSPPy-g-$C_3N_4H^+$/GCE (curve f). The enhanced electrocatalytic behavior is due to the synergetic effect of ChOx and CSPPy-g-$C_3N_4H^+$ that increases conductivity and electrocatalytic activity for cholesterol detection. Also, the hybrid composite provides large active sites for sufficient enzyme loading and short pathways for charge/electron transport, which help to electro-catalyze the cholesterol within short period of time. Additionally, CVs of ChOx-CSPPy-g-$C_3N_4H^+$/GCE was measured in the presence of 0.05 mM cholesterol at different scan rates (25–250 mV/s), as illustrate in Fig. 4(ii). The calibrated plot of redox peaks current as shown in inset of Fig. 4(ii), demonstrate the current vs. square root of scan rate with high correlation coefficient value (R^2 =0.9954), which confirms that the electrochemical kinetics of redox reactions are confined to electrode active surface.

3.2.4. Amperometric response of the ChOx-CSPPy-g-$C_3N_4H^+$/GCE biosensors

Amperometric measurements were performed to evaluate the sensing performance of as fabricated ChOx-CSPPy-g-$C_3N_4H^+$/GCE biosensor obtained by successive addition of varying concentration of cholesterol in 0.1 M PBS (pH 7.4) at an applied constant potential of +0.17 V (vs. SCE) under stirring, as shown in Fig. 5a. As we could see that, there was steeply increase in current with increasing cholesterol concentration (see inset of Fig. 5a). From typical current-time (*i*-t) curve (Fig. 5a), the biosensor exhibited rapid and prominent increase in current response, which achieved current stability in ~3 s. The results demonstrate that ChOx-CSPPy-g-$C_3N_4H^+$/GCE biosensor has excellent catalytic activity and sensitivity towards different concentration of cholesterol. Fig. 5b shows the calibration curve of amperometric response of the biosensor exhibits a linear increase of oxidation current with increasing cholesterol concentration in the range of 0.02–5.0 mM with a low detection limit of 8.0 μM (based on the signal and noise ratio (S/N) of 3) which is more wider than other reported 2D material based biosensors (Lin et al., 2016; Gholivand and Khodadadian, 2014). As fabricated ChOx-CSPPy-g-$C_3N_4H^+$/GCE biosensor exhibited higher sensitivity (645.7 $\mu A mM^{-1}$ cm^{-2}), evaluated from the regression coefficient (R^2 =0.9988) of the linear part of the calibrated curve i.e. y=8.768+45.194x, where y is current in μA and x is the cholesterol concentration in mM. Further, the Michaelis-Menten constant (K *app/M*) was calculated using Lineweaver-Burk equation (Pang et al., 2012), $1/i$=(K *app/M* $/i_{max}$) (1/C) +$1/i_{max}$)), where *i*, i_{max} and C correspond to the steady- state catalytic current after the addition of substrate concentration, maximum current measured under saturation of enzyme-substrate reaction, and concentration of substrate, respectively. The estimated K *app/M* value was 0.052 mM (Fig. 5c) which is lower than most of the previously reported cholesterol biosensors (see Table S1, Supplementary material), suggesting the strong affinity of enzyme-cholesterol reaction and high sensing performance of our biosensor. From Table S1, it is evident that sensitivity of our electrodes are significantly higher in wide linear range than previously reported polymer based cholesterol biosensors. Additionally, in comparison with only nanomaterial based cholesterol biosensor, which showed better sensitivity but narrow linear detection range. The enhanced sensing performance can be attributed to the oxidized CSPPy decorated on ultra-thin surface functionalized 2D g-$C_3N_4H^+$ through π-conjugated bonds, which effectively maximize the electrical conductivity and improve the enzyme immobilization capacity.

3.3. Anti-interference, reproducibility, repeatability, and long-term stability of biosensors

Various potential interfering species (i.e. glucose, uric acid (UA), ascorbic acid (AA), dopamine (DA) and L-cysteine (L-Cyst)) present in human blood are easily oxidized at lower potential voltage, resulting increase in oxidation current that causes interference during detection

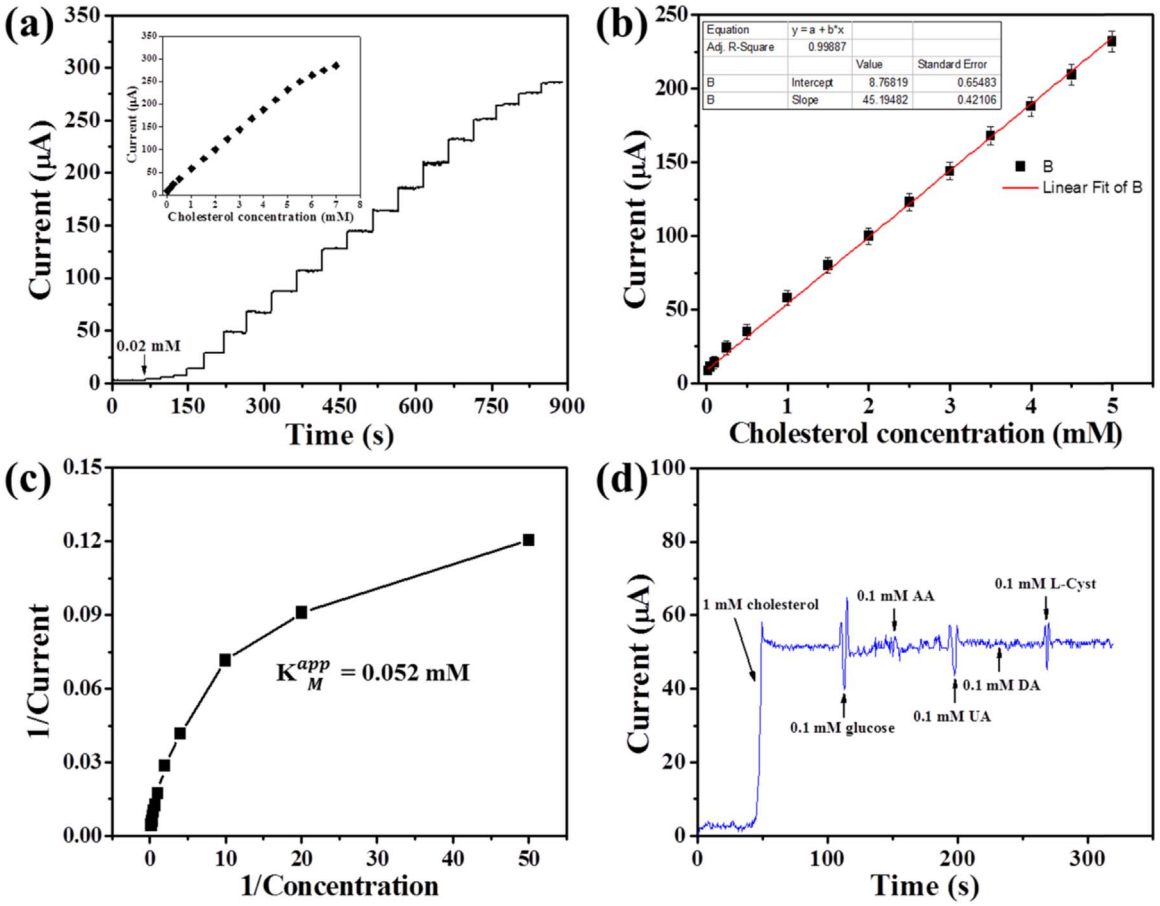

Fig. 5. (a) Amperometric response of the ChOx-CSPPy-g-$C_3N_4H^+$/GCE biosensor at +0.17 V with successive addition of different cholesterol concentrations (0.02–7.0 mM) in 0.1 M PBS while stirring; (b) Calibration curve of amperometric response showing linearity; (c) Lineweaver-Burk plot; and (d) Anti-interference test. Inset a shows the overall calibration curve of amperometric response.

of particular biomolecules (i.e. cholesterol). As shown in Fig. 5d during anti-interference ability test, ChOx-CSPPy-g-$C_3N_4H^+$/GCE biosensor showed a quick and significant increase in current response after 1 mM cholesterol addition, whereas an addition of 0.1 mM of each analytes such as glucose UA, AA, DA, and L-Cyst in 0.1 M PBS (pH 7.4) did not cause any noticeable change in current response at applied a potential of +0.17 V during amperometric measurement suggesting the biosensor exhibited good anti-interference behavior. The favourable selectivity can be ascribed to the enzyme-substrate affinity and anti-interference behavior of composite material.

The reproducibility of the fabricated biosensor (ChOx-CSPPy-g-$C_3N_4H^+$/GCE) electrode was measured by comparing the response of six similarly prepared biosensor electrodes under same condition in the presence of 1 mM cholesterol in 0.1 M PBS (pH 7.4). The relative standard deviation (RSD) was found to be ≤3.7%, which indicated the great reproducibility of the biosensors. Additionally, repeatability of the biosensor was also monitored for ten repeated measurements, which showed an average RSD of ≤3.46%, confirming that biosensor electrode exhibited excellent repeatability. Furthermore, the long-term storage stability was investigated by every three day measuring biosensor current response to 1.0 mM cholesterol 0.1 M PBS (pH 7.4). After 45th day of measurement, the biosensor retained 94% of its initial response indicating good storage stability.

3.4. Real sample analysis

To check the reliability and feasibility of the ChOx-CSPPy-g-$C_3N_4H^+$/GCE biosensor, the practical application was monitored in human serum sample. The recovery of cholesterol was measured by adding different cholesterol concentrations (i.e. 1 mM, 2 mM, and 3 mM) in ten times diluted serum sample with 0.1 M PBS (pH 7.4). The recovery was calculated after measuring the cholesterol concentration in serum containing known concentration of cholesterol (5.2 mM; Sigma-Aldrich, H4522) in the human serum. The obtained data (Fig. S7) and calibrated Table S2 are presented in supplementary material. As shown in the Table S2, the recovery range was from 97% to 101%, with RSD of 1.8–2.7%, which confirmed that the fabricated electrodes could be potentially applicable for the clinical measurement of cholesterol concentration.

4. Conclusion

In summary, we demonstrated successfully for the first time, utilization of CSPPy-g-$C_3N_4H^+$ nanohybrid composite material as novel matrix for cholesterol biosensor fabrication. The engineered composite material exhibited large and effective surface area due to exfoliation of g-$C_3N_4H^+$ into ultra-thin nanosheets. Also during ChOx enzyme immobilization, positively charged CSPPy-g-$C_3N_4H^+$ composite interacts with negatively charged enzymes, which further enhance the synergetic effects for electrocatalytic ability and electro-conductive network. As a result, the fabricated biosensor electrode showed excellent performance towards cholesterol detection with a high sensitivity (645.7 $\mu A mM^{-1} cm^{-2}$) and wide linear range (0.02–5.0 mM), low detection limit (8 μM), good selectivity, reproducibility, repeatability, and long-term stability. Additionally, cholesterol was selectively and accurately detected in human serum samples.

Acknowledgements

This paper was supported by grant from the Basic Science Research Program through National Research Foundation of Korea (NRF) by Ministry of Education, Science and Technology (Project no. 2016R1A2A2A07005160).

Appendix A. Supporting information

Supplementary data associated with this article can be found in the online version at doi:10.1016/j.bios.2017.03.072.

References

Ahmad, R., Tripathy, N., Hahn, Y.-B., 2013. Biosens. Bioelectron. 45, 281–286.
Ahmad, R., Tripathy, N., Kim, S.H., Umar, A., Al-Hajry, A., Hahn, Y.-B., 2014. Electrochem. Commun. 38, 4–7.
Ahmadalinezhad, A., Chen, A., 2011. Biosens. Bioelectron. 26, 4508–4513.
Ahuja, T., Mir, I.A., Kumar, D., Rajesh, 2007. Biomaterials 28, 791–805.
Arsenault, B.J., Puri, R., 2016. J. Thorac. Dis. 8, 2340–2343.
Aydemir, N., Malmstrom, J., Travas-Sejdic, J., 2016. Phys. Chem. Chem. Phys. 18, 8264–8277.
Bai, X., Yan, S., Wang, J., Wang, L., Jiang, W., Wu, S., Sun, C., Zhu, Y., 2014. J. Mater. Chem. A 2, 17521–17529.
Baigent, C., Blackwell, L., Emberson, J., Holland, L.E., Reith, C., Bhala, N., Peto, R., Barnes, E.H., Keech, A., Simes, J., Collins, R., 2010. Lancet 376, 1670–1681.
Brahim, S., Narinesingh, D., Guiseppi, A., 2001. Anal. Chim. Acta 448, 27–36.
Bredas, J.F., Street, G.B., 1985. Acc. Chem. Res. 18, 309–315.
Cao, J., Wang, Y., Chen, J., Li, X., Walsh, F.C., Ouyang, J.-H., Jia, D., Zhou, Y., 2015. J. Mater. Chem. A 3, 14445–14457.
Fang, W., Deng, Y., Tang, L., Zeng, G., Zhou, Y., Xie, X., Wang, J., Wang, Y., Wang, J., 2016. J. Colloid Interface Sci. 490, 834–843.
Fang, Y.A., Ferrie, M., Li, G., 2006. Biochim. Biophys. Acta 1763, 254–261.
Gholivand, M.B., Khodadadian, M., 2014. Biosens. Bioelectron. 53, 472–478.
Gong, K., Du, F., Xia, Z., Durstock, M., Dai, L., 2009. Science 323, 760–764.
Hahn, Y.-B., Ahmad, R., Tripathy, N., 2012. Chem. Commun. 48, 10369–10385.
Kofuji, Y., Isobe, Y., Shiraishi, Y., Sakamoto, H., Tanaka, S., Ichikawa, S., Hirai, T., 2016. J. Am. Chem. Soc. 138, 10019–10025.
Komathi, S., Muthuchamy, N., Lee, K.P., Gopalan, A.I., 2016. Biosens. Bioelectron. 84, 64–71.
Labarthe, D.R., Dunbar, S.B., 2012. Circulation 125, 2667–2676.
Labib, M., Sargent, E.H., Kelley, S.O., 2016. Chem. Rev. 116, 9001–9090.
Li, X.-G., Li, A., Huang, M.-R., Liao, Y., Lu, Y.-G., 2010. J. Phys. Chem. C. 114, 19244–19255.
Lin, X., Ni, Y., Kokot, S., 2016. Sens. Actuators B: Chem. 233, 100–106.
Lotsch, B.V., Döblinger, M., Sehnert, J., Seyfarth, L., Senker, Oeckler, J.O., Schnick, W., 2007. Chem. Eur. J. 13, 4969–4980.
Lu, Q., Deng, J., Hou, Y., Wang, H., Li, H., Zhang, Y., 2015. Chem. Commun. 51, 12251–12253.
Lu, Q., Wang, H., Liu, Y., Hou, Y., Li, H., Zhang, Y., 2017. Biosens. Bioelectron. 89, 411–416.
Ma, T.Y., Tang, Y., Dai, S., Qiao, S.Z., 2014. Small 10, 2383–2389.
Malhotra, B.D., Chaubey, A., Singh, S.P., 2006. Anal. Chim. Acta 578, 59–74.
Mansano, F.V., Kazaoka, R.M.A., Ronsein, G.E., Prado, F.M., G.-M, T. C, Uemi, M., Mascio, P.D., Miyamoto, S., 2010. Anal. Chem. 82, 6775–6781.
Medintz, I.L., Uyeda, H.T., Goldman, E.R., Mitosis, H., 2005. Nat. Mater. 4, 435–446.
Niu, P., Zhang, L., Liu, G., Cheng, H.M., 2012. Adv. Funct. Mater. 22, 4763–4770.
Ong, W.-J., Tan, L.-L., Chai, S.-P., Yong, S.-T., Mohamed, A.R., 2015. Nano Energy 13, 757–770.
Pang, X., Imin, P., Zhitomirsky, I., Adronov, A., 2012. J. Mater. Chem. 22, 9147–9154.
Qian, T., Yu, C., Zhou, X., Ma, P., Wu, S., Xu, L., Shen, J., 2014. Biosens. Bioelectron. 58, 237–241.
Quigley, A.F., Razal, J.M., Thompson, B.C., Moulton, S.E., Kita, M., Kennedy, E.L., Clark, G.M., Wallace, G.G., Kapsa, R.M., 2009. Adv. Mater. 21, 4393–4397.
Ramendra, S.D., Raj, C.R., 2010. J. Phys. Chem. C 114, 21427–21433.
Sadki, S., Schottland, P., Brodie, N., Sabouraud, G., 2000. Chem. Soc. Rev. 29, 283–293.
Saxena, U., Das, A.B., 2016. Biosens. Bioelectron. 75, 196–205.
Shi, Y., Wang, B., Duan, L., Zhu, Y., Gui, Z., Yuen, R.K.K., Hu, Y., 2016. Ind. Eng. Chem. Res. 55, 7646–7654.
Shklovskii, B.I., Efros, A.L., 2013. Springer-Business Media.
Shrestha, B.K., Ahmad, R., Mousa, H.M., Kim, I.-G., Kim, J.I., Neupane, M.P., Park, C.H., Kim, C.S., 2016. J. Colloid Interface Sci. 482, 39–47.
Somers, R.C., Bawendi, M.G., Nocera, D.G., 2007. Chem. Soc. Rev. 36, 579–591.
Tan, X., Li, M., Cai, P., Luo, L., Zou, X., 2005. Anal. Biochem. 337, 111–120.
Wang, K., Li, Q., Liu, B., Cheng, B., Ho, W., Yu, J., 2015. Appl. Catal. B: Environ. 176–177, 44–52.
Wang, X., Maeda, K., Chen, X., Takanabe, K., Domen, Hou, K.Y., Fu, X., Antonietti, M., 2009. J. Am. Chem. Soc. 131, 1680–1681.
Wilson, G.S., Hu, Y., 2000. Chem. Rev. 100, 2693–2704.
Wu, G., Hu, Y., Liu, Y., Zhao, J., Chen, X., Whoehling, V., Plesse, C., Nguyen, G.T.M., Vidal, F., Chen, W., 2015. Nat. Commun. 6, 7258.
Xiong, M., Rong, Q., Meng, H.-M., Zhang, X.-B., 2017. Biosens. Bioelectron. 89, 212–223.
Yuan, X., Ding, X.-L., Wang, C.-Y., Ma, Z.-F., 2013. Energy Environ. Sci. 6, 1105–1124.
Zhang, J., Chen, X., Takanabe, K., Maeda, K., Domen, K., Epping, J.D., Fu, X., Antonietti, M., Wang, X., 2010. Angew. Chem. Int. Ed. 49, 441–444.
Zhang, M., Ye, X., Qiu, X., Lin, S., Wang, X., 2014. Adv. Mater. 26, 805–809.
Zhang, Y., Thomas, A., Antonietti, M., Wang, X., 2009. J. Am. Chem. Soc. 131, 50–51.